


Nonlinear all-optical modulator based on non-Hermitian PT symmetry

HONGBIN MA,^{1,2,3} DONGDONG LI,^{1,2,3} NANXUAN WU,^{1,2,3} YIYUN ZHANG,^{1,2,3} HONGSHENG CHEN,^{1,2,3,4} AND HAOLIANG QIAN^{1,2,3,5} 

¹Interdisciplinary Center for Quantum Information, State Key Laboratory of Modern Optical Instrumentation, College of Information Science and Electronic Engineering, Zhejiang University, Hangzhou 310027, China

²ZJU-Hangzhou Global Science and Technology Innovation Center, Key Laboratory of Advanced Micro/Nano Electronic Devices & Smart Systems of Zhejiang, Zhejiang University, Hangzhou 310027, China

³International Joint Innovation Center, ZJU-UIUC Institute, Zhejiang University, Haining 314400, China

⁴e-mail: hansomchen@zju.edu.cn

⁵e-mail: haoliangqian@zju.edu.cn

Received 8 December 2021; revised 30 January 2022; accepted 14 February 2022; posted 15 February 2022 (Doc. ID 450747); published 25 March 2022

All-optical modulators with ultrahigh speed are in high demand due to the rapid development of optical interconnection and computation. However, due to weak photon–photon interaction, the advancement of all-optical modulators is consequently hampered by the large footprint and high power consumption. In this work, the enhanced sensitivity around an exceptional point (EP) from parity-time (PT) symmetry theory is initiatively introduced into a nonlinear all-optical modulator design. Further, a non-Hermitian all-optical modulator based on PT symmetry is proposed, which utilizes the large Kerr nonlinearity from indium tin oxide (ITO) in its epsilon-near-zero (ENZ) region. The whole system is expected to operate around EP, giving rise to the advantages of nanoscale integration and large modulation depth. This presented modulator with high efficiency and high-speed all-optical control can be commendably extended to the design methodology of various nanostructures and further prompt the development of all-optical signal processing. © 2022 Chinese Laser Press

<https://doi.org/10.1364/PRJ.450747>

1. INTRODUCTION

Optical modulators play a crucial role in photonic integrated circuits (PICs) for optical interconnection and computation under the circumstance of ever-growing data traffic [1–3]. In recent years, a variety of electro-optic modulators have been reported, which are implemented on several platforms such as an InGaAsP/Si hybrid metal-oxide–semiconductor [4,5] and classical nonlinear crystals that include lithium niobate [6,7]. However, most of these modulators have issues of large footprint (tens or hundreds of micrometer level) or limited modulation-speed at the GHz level. Over the past few years, all-optical modulators have emerged with higher operating speeds than their electronic counterparts [8,9]. Yet, the weak photon–photon interaction remains an impediment for all-optical device design. Thus, for higher compactness and efficiency, optimized photonic structures with strong optical nonlinear interaction are necessary. Currently, epsilon-near-zero (ENZ) materials that exhibit a vanishing real part of the permittivity in a certain wavelength range have emerged with ultrahigh nonlinear response [10]. As a key member of ENZ materials, ITO has been extensively applied in optical modulators with its active electro-variable refractive index [11–13].

However, the large optical third-order nonlinearity from ITO at the ENZ region, which may bring large modulation depth and high modulation speed, has hardly been utilized in modulators hitherto. Moreover, in addition to the nonlinear coefficient of the material itself, efficient nonlinearity is also affected by the photonic structural design. Under this circumstance, recent exploration of the enhanced sensitivity from an exceptional point (EP) in parity-time (PT) symmetry theory may offer a novel approach.

The concept of PT symmetry effectively describes the existence of completely real spectra for non-Hermitian Hamiltonians with complex conjugation potential as $V(x) = V^*(-x)$ [14]. PT-symmetric Hamiltonians can undergo a phase transition to a symmetry-broken regime, where complex eigenvalues appear formally through a parametric variation [15]. This kind of transition point could be manifested by the properties of EP, which are initiated in the studying of non-Hermitian operators. At the EP, both the eigenvalues and eigenstates coalesce [16]. It has been proved that an elaborate parametric design would lead systems to operate around EP and exhibit enhanced sensitivity [17–20]. For the past decade, non-Hermitian physics and PT symmetry have prompted

novel micro-nano devices with high performance, for instance, nonreciprocal resonators [21,22], PT-symmetric lasers [23,24], and non-Hermitian electromagnetic metasurfaces [25]. Tunable effects of PT symmetry have exhibited signs of applications, including 1D and 2D photonic lattice geometries through tuning the complex refractive index [26–28], single-mode laser through manipulating the gain/loss of a microring resonator [29], and light-light switching through interferometrical manipulation [30]. However, most of these cases contain the gain media that are difficult to be applied in high-speed all-optical control [31–33]. Further, PT symmetry theory has yet to be practically introduced into the design of nonlinear all-optical modulators. It is known that, during the optimization of a modulator, plenty of attempts and simulations are always repeated with different geometric parameters in order to attain the optimum performance. By contrast, the EP may reasonably explicate the optimizing process and make it straightforward to improve the modulation depth and reduce the device footprint.

Here, we propose a non-Hermitian all-optical modulator based on PT symmetry utilizing the large optical nonlinearity from ITO in its ENZ region to tune the coupling coefficient between two waveguides. This optical modulator is designed to operate around EP and achieve THz-level switching through an external femtosecond pump laser, leading to the advantages of nanoscale integration, large modulation-depth, and high-speed all-optical control. To the best of our knowledge, it is the first time that the practical application based on PT symmetry is demonstrated for nonlinear all-optical modulators. The presented structure is composed of conventional materials such as silicon and cobalt, which have good compatibility toward CMOS fabrication technologies. Also, our work identifies a method of optimization for nanostructures using PT symmetry theory, which could be directly extended to the PIC platform and provides a new impetus for the development of all-optical applications.

2. THEORY DEMONSTRATION AND THE PROPOSED MODULATOR

By analogy with the complex conjugation potential, for a PT-symmetric optical system, its refractive index distribution should be complex conjugated, namely, $n(x) = n^*(x)$. Thus, for conventional two-coupled waveguides or resonator structures, the balance between gain and loss plays a major role.

However, due to the requirement of sustained external power and the accompanying high energy consumption, gain media are not practical for efficient and high-speed on-chip integrated modulators. Fortunately, the definition of PT symmetry has been successfully generalized to passive systems that include loss-only structures, and the low-loss (or lossless) part could be considered as a gain part through a change of reference point (loss offset); thus, the general non-Hermitian system (H_0) could be taken part into a PT-symmetric coupled subsystem (H_{PT}) and a decaying subsystem (H_L) [34]. Two coupled waveguides as lossless and lossy ones are utilized for illustration, as shown in Fig. 1(a). Optical-field dynamics in such a straight-forward system could be characterized by the coupled-mode theory, from which a Hamiltonian H_0 is obtained [35]:

$$H_0 = H_L + H_{PT} = \begin{bmatrix} -\frac{1}{2}i\gamma_0 & 0 \\ 0 & -\frac{1}{2}i\gamma_0 \end{bmatrix} + \begin{bmatrix} \beta_0 + \frac{1}{2}i\gamma_0 & \kappa_0 \\ \kappa_0 & \beta_0 - \frac{1}{2}i\gamma_0 \end{bmatrix}, \quad (1)$$

where β_0 is the propagation constant of two waveguides, γ_0 is the propagation loss of the lossy waveguide, and κ_0 denotes the coupling coefficient. Correspondingly, the eigenvalues of the PT-symmetric-coupled subsystem can be represented as

$$\lambda_{1,2} = \text{Re}\left(\beta_0 - \frac{1}{2}i\gamma_0\right) \pm \frac{1}{2}\sqrt{4\kappa_0^2 - \gamma_0^2}. \quad (2)$$

Note that $\text{Im}(\beta_0 - \frac{1}{2}i\gamma_0)$ refers to the decaying subsystem mentioned above. Apparently, PT symmetry would be broken when $\lambda_{1,2}$ becomes complex, namely, $\gamma_0 > 2\kappa_0$ beyond EP ($\gamma_0 = 2\kappa_0$). Figures 1(b) and 1(c) exhibit the Riemannian surfaces of the complex eigenvalues that vary with κ_0 and γ_0 . For a better demonstration and understanding, these surfaces contain the situations when $\gamma_0 < 0$ or $\kappa_0 < 0$, while the primary concern for this coupled-waveguides system is when both parameters are greater than zero. Given a designated κ_0 , when γ_0 keeps increasing and arrives above the transition point (boundary of red and blue regions), the real spectrum coalesces while the imaginary one bifurcates; thus, the system's mode experiences different attenuation at the location of each waveguide (the most intuitive phenomenon, so-called “loss-induced transparency,” is that the transmitted light in a lossless waveguide increases as γ_0 increases) [36]. As a consequence, the red regions

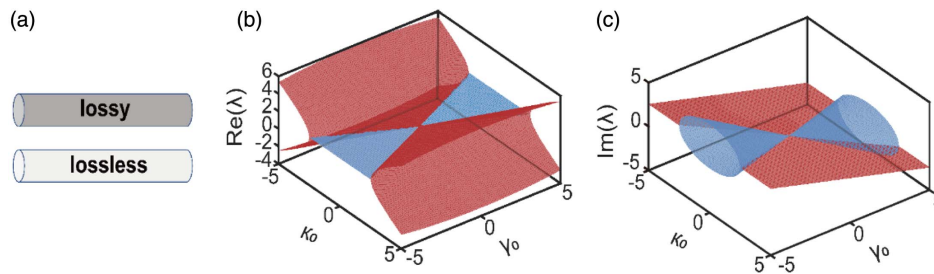


Fig. 1. Coupled-waveguides system with its representation of the complex eigenvalues as Riemannian surfaces. (a) Two coupled waveguides, as lossless and lossy ones, respectively, form an integrated system that possesses a Hamiltonian H_0 . (b), (c) Riemannian surfaces of the complex eigenvalues [real (b) and imaginary (c) parts] of the matrix H_0 versus the (κ_0, γ_0) parameters, where the blue regions represent PT-broken and red ones are PT-symmetric regions. In addition, the boundary is considered as lines of EPs. Notably, these Riemannian surfaces contain the PT-symmetric coupled subsystem and decaying subsystem for a realistic manifestation. The existence of a decaying subsystem causes a tilt angle for the surface in (c).

mean PT symmetry, while blue regions are PT-broken, and the intersections of the surface are the lines of EPs, where both eigenstates and eigenvectors become degenerate. Certainly, changing the value of κ_0 under a settled γ_0 also has a similar effect. Moreover, owing to the sensitivity provided by the bifurcation properties of non-Hermitian degeneracies, a little variation of κ_0 would lead to a radical change for the whole system [37]. Thus, to construct a nanoscale modulator working around EPs, through tuning the coupling coefficient between waveguides and delicately designing the loss distribution, has shown an unlimited source of fascination.

The proposed modulator integrated on SiO_2 substrate is presented in Fig. 2(a), which comprises an ITO layer sandwiched by a lossless propagating waveguide and a hybrid lossy waveguide. The propagating waveguide is totally composed of silicon (Si_{wide}), while the hybrid lossy waveguide consists of silicon ($\text{Si}_{\text{narrow}}$) and cobalt. Here, cobalt is exploited to break through the limitation of Kramers–Kronig relations owing to its similar real part of refractive index to silicon and a large extinction coefficient, which reduces the detuning between two waveguides while leading to heavy loss [38,39]. In order to utilize the large Kerr coefficient from ITO and distinguish the signal and pump, the signal wavelength is set as 1240 nm (ENZ wavelength), while the pump is chosen at 1250 nm according to one of the previous reports on ITO's Kerr nonlinearity, where the change of the refractive index is from $n_0 = 0.42 + 0.42i$ to $n_l = 1.14 + 0.27i$ with 30° incident pump [40]. Note that the operating wavelength at 1240 nm is deduced from current data, and this wavelength could be moved to 1550 nm telecom wavelength through changing ITO's annealing temperature and doping concentration [41]. In our work, ITO is expected to realize the alteration of a coupling coefficient through its different refractive index with and without the pump laser. With regard to the modulation mechanism, on the one hand, ITO would involve in the light–matter

interaction when a pump laser is applied, leading to an increased real part of refractive index and a decreased imaginary part. With the reduced difference between the refractive indexes of ITO and silicon, propagating light will be coupled into the hybrid lossy waveguide and decay consequently, which results in an off-state. On the other hand, the system is working on-state without a pump. These two states are plotted as power-flow at xy and yz planes, as shown in Figs. 2(b) and 2(c). Apparently, a portion of power-flow is distributed in ITO and the hybrid lossy waveguide at the off-state, indicating the light-field coupling and sharp attenuation. Here, the on-state transmitted power efficiency (the ratio of output and input power) is about 50.69%, while the off-state one is 10.68%, which gives the extinction ratio of 6.46 dB.

It has been proved that, for an ITO–air interface case, the electric-field components (normal to the interface) in ITO are inversely proportional to the permittivity of ITO because of the continuous displacement field; thus, the electric field would be enhanced at the ENZ region with an obliquely incident light [40]. The calculation result of electric-field enhancement in ITO at the xz plane is shown in Fig. 2(d). The maximum electric-field enhancement inside ITO reaches up to 31 times, and the average enhancement is about 14 times. This enhancement boosts the third-order optical nonlinear interactions in ITO, contributing to enlarging the variation of the linear refractive index at lower pumping power [42]. Note that the nonlinear optical coefficients of silicon [43] and cobalt [44] are several orders of magnitude smaller than that of ITO at the ENZ wavelength; thus, the nonlinear responses of silicon and cobalt are not under consideration.

3. RESULTS AND SYSTEM ANALYSIS

For the whole system of the non-Hermitian modulator, here the conventional coupled-mode-theory is used (see Appendix C

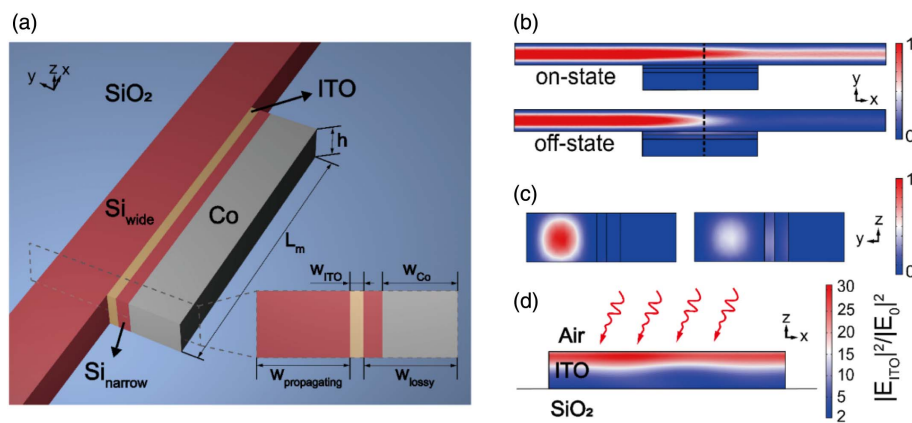


Fig. 2. Schematics of the proposed modulator, internal electric-field, and power-flow distribution. (a) Structure of modulator integrated on SiO_2 (blue) substrate. ITO (yellow) is sandwiched between the propagating waveguide composed of Si_{wide} and hybrid lossy waveguide composed of $\text{Si}_{\text{narrow}}$ and cobalt (gray). Note that both red regions represent silicon. Inset shows the cross-section at the yz plane. Widths of propagating and hybrid lossy waveguides are set to be the same, namely, $W_{\text{propagating}} = W_{\text{lossy}} = 280$ nm. Besides, $W_{\text{ITO}} = 40$ nm and $W_{\text{Co}} = 224$ nm are the width of ITO and cobalt, respectively. Furthermore, ITO and two waveguides are designed with the same height $h = 200$ nm. Last, the modulation length is considered to be within one wavelength, $L_m = 1240$ nm. (b), (c) Power-flow in the modulator at on-state and off-state from xy plane and yz plane views. The black dashed lines in (b) mark the location of the yz -plane view in (c), where the coupled energy in hybrid lossy waveguide reaches the maximum. (d) Field enhancement at the central cross-section at xy plane in ITO. Pump laser (1250 nm, 30° incident angle) marked as red spiral curves is imposed on ITO. E_{ITO} means the electric field at ITO and E_0 is the incident electric field.

for its reasonability in this system), and the optical-field dynamics can be represented by coupled mode equations as

$$i \frac{dA_1(x)}{dx} = (\beta_1 - i\gamma_1)A_1(x) + \kappa_{12}A_2(x), \quad (3)$$

$$i \frac{dA_2(x)}{dx} = (\beta_2 - i\gamma_2)A_2(x) + \kappa_{21}A_1(x), \quad (4)$$

where $A_1(x)$ is the optical field amplitude, β_1 and γ_1 are the propagation constant and propagation loss in propagating waveguide, respectively, while $A_2(x)$, β_2 , and γ_2 correspond to the ones in a hybrid lossy waveguide. In addition, κ_{12} means the energy coupled from a hybrid lossy waveguide to propagating waveguide and κ_{21} vice versa. Note that κ_{12} would equal κ_{21} only when the two waveguides are set to the same [45]. Here, the detuning parameter of the waveguides is set as $\delta = \beta_1 - \beta_2$, which is close to zero when the refractive indexes of two waveguides are equivalent. In the calculation, due to the similarity of cobalt and silicon for their real parts of refractive index, δ is

supposed to be near-zero, leading to an approximative condition of $\kappa = \kappa_{12} = \kappa_{21}$ (κ will be referred to as the coupling coefficient in the following discussion). Subsequently, system's Hamiltonian comes to be a new one as

$$H_1 = \begin{bmatrix} \beta_1 - i\gamma_1 & \kappa \\ \kappa & \beta_2 - i\gamma_2 \end{bmatrix}. \quad (5)$$

Similarly, the eigenvalue of the whole system can be calculated as

$$\lambda'_{1,2} = \frac{1}{2}[(\beta_1 - i\gamma_1) + (\beta_2 - i\gamma_2)] \pm \frac{1}{2}\sqrt{4\kappa^2 - (\gamma_1 - \gamma_2)^2}. \quad (6)$$

Hence, a quantitative judgment method could be deduced to determine which state the modulator operates at. When $\kappa > \frac{1}{2}|\gamma_1 - \gamma_2|$, the system is PT-symmetric. On the contrary, when $\kappa < \frac{1}{2}|\gamma_1 - \gamma_2|$, it is at the PT-broken state. Certainly, the point where both of them are equal is expected as EP.

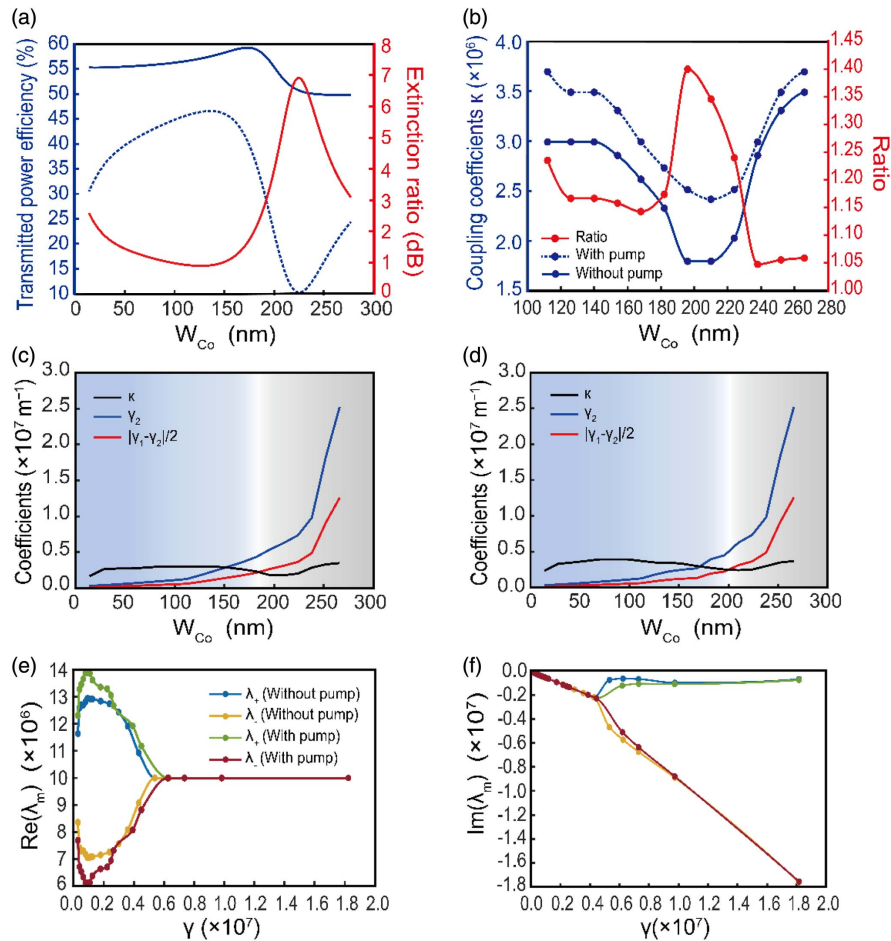


Fig. 3. Analysis of PT-symmetric and PT-broken regions and eigenvalue spectra of the whole modulator system. (a) Transmitted power efficiency varies with W_{Co} from 14 to 280 nm. The blue dashed and solid curves mean systems with and without pump, respectively. The red curve represents the calculated extinction ratio. (b) The calculated coupling coefficients κ with pump (blue dashed curve) and without pump (blue solid curve). The range of W_{Co} is captured from 112 to 266 nm to study the change of κ around EP. The red curve presents the ratio of coefficients with and without pump. (c), (d) The W_{Co} dependent κ (black curve) and the propagation loss of hybrid waveguide γ_2 (blue curve) (c) without pump and (d) with pump. The red curve that represents $|\gamma_1 - \gamma_2|/2$ is designed to compare with κ to judge whether the system is in the status of PT-symmetric (blue regions) or PT-broken (gray regions). (e), (f) The relative-loss $\gamma = |\gamma_1 - \gamma_2|$ dependent eigenvalue spectra of the system. Four legends with different colors mark the eigenvalues with and without pump. Due to the fluctuation of coupling coefficient, the spectra are not smooth as expected.

To search for the EP, the simulation of W_{Co} -dependent transmitted power efficiency of the propagating waveguide with and without a pump has been carried out and plotted, as shown in Fig. 3(a). In order to keep the approximation ($\delta \sim 0$) valid, the sum of W_{Co} and the width of Si_{narrow} are set to be invariant, which means the condition of $W_{propagating} = W_{lossy} = 280$ nm is always the same. Clearly, the dashed and solid blue curves decrease sharply when W_{Co} reaches up to 160 nm. Further, the ascending transmission efficiency above 224 nm induced by the increasing loss corresponds to the “loss-induced transparency” [36]. It can be inferred that EP should be around 224 nm where the extinction ratio reaches the maximum. Note that the abnormal increasing trend of the transmitted power efficiency before 160 nm is mainly caused by the influence of the gap mode as produced in Si_{narrow} (see in Appendix B). To study the coupling mechanism around EP, the quantitative calculation for coupling coefficient κ with and without pump is plotted in Fig. 3(b). For a better comparison, the coupling-coefficient ratio (division of coefficients with pump and without pump) is calculated and shown as the red curves. The coupling-coefficient ratio around EP presents a sharp peak, corresponding to an increase of extinction ratio.

To further verify the accurate location of EP, calculation for propagation loss is absolutely necessary. Considering the existence of attenuation at on-state (mainly caused by loss of ITO), an approximative approach is adopted to divide ITO in half and distribute them into two waveguides (see in Appendix C for the calculation method). Then, the propagation loss of a hybrid lossy waveguide is presented as γ_2 , and the γ_1 is for the propagation loss of the propagating waveguide caused by the half of ITO. The PT-symmetric and PT-broken regions attained from the comparison of $\frac{1}{2}|\gamma_1 - \gamma_2|$ and κ are plotted in Fig. 3(c) (without pump) and Fig. 3(d) (with pump). Deduced from the intersection point of the red and black curves, the location of EP has a change from 184 nm (without pump) to 201 nm (with pump). The system has been actually PT-broken, even when extinction ratio has not risen to the maximum. In fact, the sensitivity is significantly enhanced near the transition point from the PT-symmetric to PT-broken regime, not actually the EP [17]; further, the near-EP region has been commonly utilized in device design [46–48]. Thus, performing the mode switching or modulation operation does not require crossing the EP, and it would be reasonable to set modulator’s operating point at the PT-broken state (near EP) in

consideration of high extinction ratio. Given all this, the real and imaginary spectra of systems’ eigenvalues with and without a pump have been calculated according to Eq. (6) in Figs. 3(e) and 3(f). For a better demonstration, here $\gamma = |\gamma_1 - \gamma_2|$ is utilized as the unit of horizontal coordinate-axis. The calculated results commendably match the analysis of Riemannian surfaces in Fig. 1.

The influence of W_{ITO} on the modulator’s extinction ratio and on-state transmitted efficiency is studied as shown in Figs. 4(a) and 4(b). The trends of these two performance parameters are nearly opposite under the variation of W_{ITO} (the larger extinction ratio, the lower on-state transmitted efficiency), which suggests that it should be necessary to balance these two parameters. Two ultimate situations when W_{ITO} is 30 and 70 nm are plotted in Figs. 4(c) and 4(d). For the case of $W_{ITO} = 30$ nm, the extinction ratio reaches 10.16 dB, and the on-state transmitted efficiency is 42.5% [Fig. 4(c)], while the extinction ratio is 3.19 dB with on-state transmitted efficiency up to 63.9% under 70 nm W_{ITO} [Fig. 4(d)]. Another decisive factor of the overall performance of modulators is modulation speed. For our structure, the modulation speed mainly depends on the group velocity in the modulation region and lifetime of the nonlinear response. As the calculation process shows in Appendix D, the propagating time is about 21.2 fs, while the recovery time of the nonlinear response in ITO is 360 fs. Thus, the recovery time is the predominant factor, which allows an all-optical modulation speed up to 2.78 THz, promising for advancement of the terahertz modulators [49,50].

4. DISCUSSION AND CONCLUSION

As described, the offset between EP and the locations of maximum extinction ratio is an inevitable challenge due to the loss of tunable material. To overcome this problem, a new method may be possibly employed to replace ITO by multiple metallic-quantum-wells (MQWs) [51,52], which could largely enhance the optical nonlinearity at the lower-loss wavelength region. On the other hand, for our tentative structure that demonstrates the application of PT symmetry on nonlinear all-optical modulator, there is still room for improvement. For example, the hybrid lossy waveguide could be placed at both sides of the propagating waveguide to achieve shorter modulation length and a more compact device, while it will introduce the

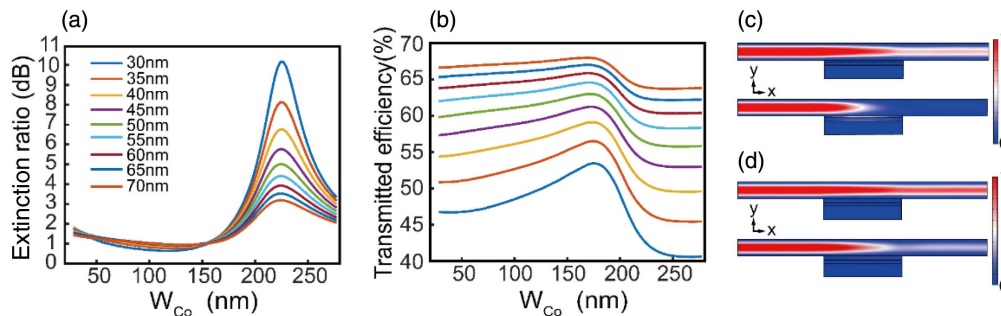


Fig. 4. Analysis of the balance between extinction ratio and on-state transmitted efficiency. (a), (b) The W_{Co} -dependent extinction ratio and on-state transmitted efficiency under different W_{ITO} from 30 to 70 nm. Note that the legends are the same for both (a) and (b). (c), (d) Two ultimate states of power-flow distribution at the xy plane where W_{ITO} is 30 nm in (c) and 70 nm in (d).

difficulty to analyze the coupling coefficient at the same time. In addition, it is also reasonable to consider the resonant ring structure [53] to further improve the performance. Furthermore, the plasmonic structures with extreme field-confinement may prospectively contribute to the advancement of extinction ratio [54,55]. In regard to fabrication of this non-Hermitian modulator, the silicon waveguide can be fabricated by the electron-beam lithography and etching process. The cobalt waveguide and ITO slot can be processed by the film deposition after the electron-beam lithography. These several rounds of processes are compatible with the standard CMOS technology, thus enabling the prospect of integration with other PIC platforms [56–58]. At last, due to the 14-times electric-field enhancement provided by the sandwich structure (waveguide, ITO, waveguide) at the ENZ wavelength, and comparing with four-times enhancement in Ref. [40], the actual requirement of incident intensity would be reduced to about 42.8 GW/cm^2 . As an example of a femtosecond laser with 100 fs pulse width, 80 MHz repetition rate, and the focused spot radius of L_m , the averaged power of 16.56 mW is supposed to be applied. Moreover, the transmitted efficiency versus pump intensity in Appendix A shows that the required power could be reduced further with slight sacrifice of extinction ratio.

In summary, we propose an all-optical modulator based on non-Hermitian PT symmetry utilizing the nonlinearity from ITO at the ENZ region. Further, it has been demonstrated that applying the supreme sensitivity around EP to the all-optical modulator would lead to performance improvement and superiority. For the presented structure, the modulation depth comes up to $5.21 \text{ dB}/\mu\text{m}$, while the on-state transmitted efficiency is 50.69%. Additionally, the modulator has a compact device footprint of $1.24 \mu\text{m} \times 0.156 \mu\text{m}$ and an ultrahigh modulation speed that is up to the THz level. Moreover, the proposed device commendably proves the practical application of EPs in on-chip integrated modulators, which would be referred and extended to the design methodology of various nanostructures and further prompt the development of all-optical communication and high-speed signal processing.

APPENDIX A: SIMULATION FOR THE WHOLE STRUCTURE

Numerical simulations using the finite element method, including the power flow in the waveguides, calculation of coupling coefficient, and loss coefficient, are performed with COMSOL Multiphysics. The 2D mode analysis presented as electric-field distribution for the input port of propagating waveguide is plotted in Fig. 5, which gives the effective mode index as $2.04 - 2.98 \times 10^{-5}i$. This calculated effective mode index is utilized for the input that is applied to the port of a propagating waveguide in 3D simulation.

As one of the important components in the device's configuration, the parameters of ITO are taken as two ultimate values. Namely, the refractive index of ITO is changed from $0.42 + 0.42i$ (without pump) to $1.14 + 0.27i$ (under 30° incident pump laser with an intensity of 150 GW/cm^2) [40]. Furthermore, the power transmission versus the pump intensity is calculated, as shown in Fig. 6. When the intensity reaches 100 GW/cm^2 , the transmitted efficiency decreases to

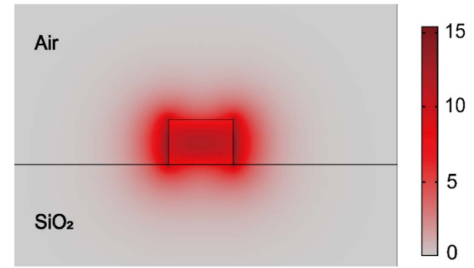


Fig. 5. Electric-field distribution of the input port for propagating waveguide.

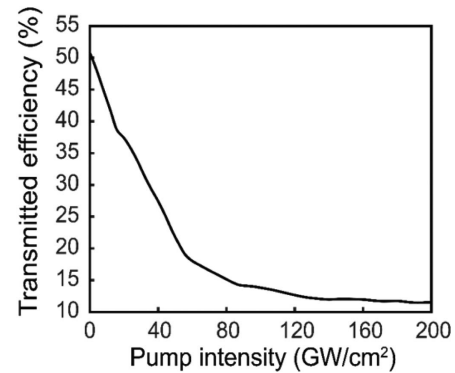


Fig. 6. Transmitted efficiency versus pump intensity.

about 10%, leading to a 5.65 dB extinction ratio. With sacrifice of the extinction ratio, the power intensity could be further reduced.

APPENDIX B: GAP MODE ANALYSIS

Figure 7(a) is the schematic of the whole system at the xy plane, where the hybrid lossy waveguide is marked by the gray dashed rectangle. The electric-field distribution with different widths of cobalt W_{Co} is plotted in Figs. 7(b)–7(i). The electric field is mainly distributed in the gap between ITO and cobalt (i.e., S_{narrow}). This gap mode contains two parts of an electric field, E_1 and E_2 , which are illustrated as black and white dashed ellipses in Fig. 7(b). Deduced from the change of the E_1 , when the W_{Co} increases (before 160 nm) and the gap becomes narrower, E_1 becomes weaker while E_2 is stronger. Although E_2 is becoming more obvious, it is not in a predominant role until the W_{Co} increases to about 160 nm. Under this circumstance, when the coupled electric field in the gap only has E_2 , the loss of cobalt would be efficiently utilized. Then, enlarging the W_{Co} can better reflect the increase of total propagation loss for the hybrid waveguide.

APPENDIX C: CALCULATION METHOD FOR COUPLING COEFFICIENT AND PROPAGATION LOSS

The modulator's Hamiltonian is deduced from the coupled mode theory (CMT). Actually, using the conventional CMT for the coupled-waveguides here may cause 1% to 2% error

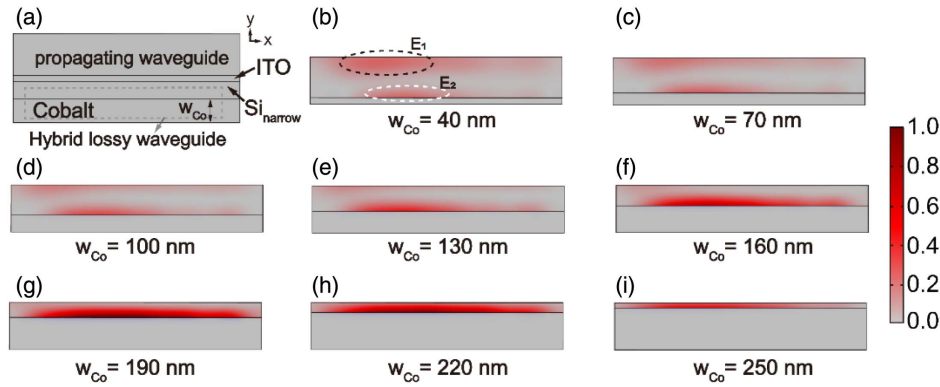


Fig. 7. Normalized electric-field distributions in the hybrid lossy waveguide. (a) Schematic of the whole system at the xy plane. Hybrid lossy waveguide composed of $\text{Si}_{\text{narrow}}$ and cobalt is marked as the gray dashed rectangle; width of cobalt is marked as w_{Co} . (b)–(i) Electric-field distributions in hybrid lossy waveguide under different w_{Co} , which is from 40 to 250 nm (as the example when ITO is under pump). Note that the electric field is mainly distributed in $\text{Si}_{\text{narrow}}$ and sorted into two parts, E_1 and E_2 , which are marked as the black and white circles, respectively, in (b).

according to Ref. [35]. However, this difference has little influence on the location of the PT-transition point (about few-nanometers offset). In addition, the sensitivity is enhanced around EP, and the whole system working conditions are demonstrated through the full-wave simulation. Moreover, we chose “conventional CMT” to better understand and demonstrate the idea of non-Hermitian modulator straightforwardly.

For the non-Hermitian PT-symmetry system, loss and the real part of refractive index are equally important; further, the coupling coefficient should be calculated at the existence of cobalt. Here, the coupling coefficient is normally characterized by the coupling length, which is defined as the distance where the maximum guided power is transferred from one waveguide to the other. Accordingly, the coupling coefficient can be represented as

$$\kappa = \frac{\pi}{2L_0}, \quad (\text{C1})$$

where L_0 is the coupling length. The simulation structure is shown in Fig. 8(a), and the modulation length is intentionally extended to 1600 nm for the calculation of coupling length. The transmitted power at each location of hybrid lossy waveguide is

calculated through the surface integral of power flow. The results are plotted in Figs. 8(b) and 8(c).

Due to the existence of loss at on-state, which is mainly caused by ITO, approximate analysis of dividing ITO into two parts has been considered. One part contributes to the propagating waveguide, and the other part to the hybrid lossy waveguide. Set γ_1 and γ_2 as the loss of propagating and hybrid lossy waveguide, respectively. The simulation structures for γ_1 and γ_2 are presented in Figs. 9(a) and 9(b). Moreover, the decay curves in the simulation structures are shown in Figs. 9(c) and 9(d). Owing to the exponential attenuation in the waveguide, here the natural exponential curve fitting is exploited to obtain the decay coefficients.

APPENDIX D: MODULATION SPEED

For the presented modulator, the modulation speed generally depends on the propagation time in the modulation region and the lifetime of nonlinear response. The speed of propagation could use the concept group velocity V_g for the description. Group velocity can be interpreted as the speed of information in a wave, which is defined as [59]

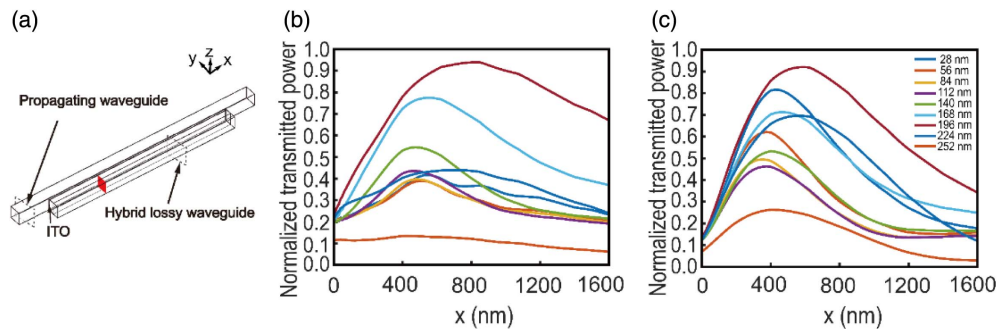


Fig. 8. Normalized transmitted power in hybrid lossy waveguide that is used for calculation of coupling coefficients. (a) Schematic of the simulation structure. The red cross section in hybrid lossy waveguide is used to calculate the surface integral of power flow at each location. (b), (c) Situations without and with pump, respectively. The x -label is the transmitted distance, and each curve means the situation for the specified width of cobalt (from 28 to 252 nm). The coupling length is exactly the distance where the transmitted power reaches the maximum.

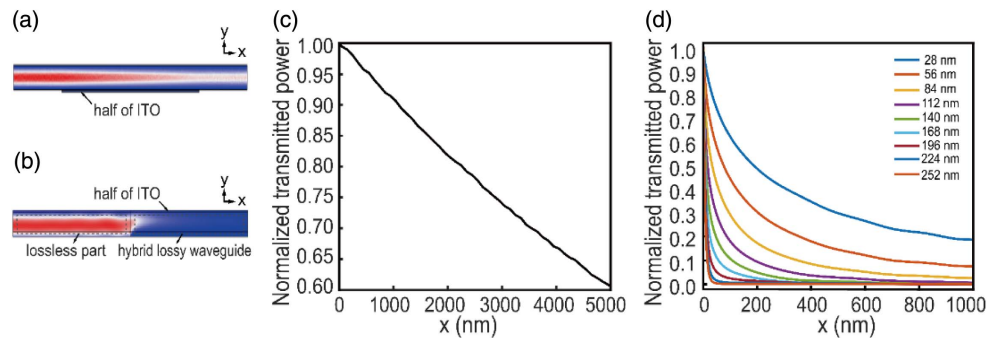


Fig. 9. Simulation structures for the calculation of propagation loss and their normalized transmitted power (as the example when ITO is under pump). (a) The propagating waveguide with a half of ITO. (b) The hybrid lossy waveguide with a half of ITO. The imaginary part of the refractive index in the left part (marked as lossless part by gray dashed rectangle) is deliberately set to be zero for the more realistic simulation of the propagating and coupling mechanism, which leads to a sharp decay when light propagates to hybrid lossy waveguide. (c), (d) The decay curves of the transmitted power in (a) and (b). The initial positions ($x = 0$) are where the propagating waveguide has ITO for (c) or at the interface of the lossless part and hybrid lossy waveguide for (d). Note that curves in (d) are presented under different widths of cobalt (from 28 to 252 nm).

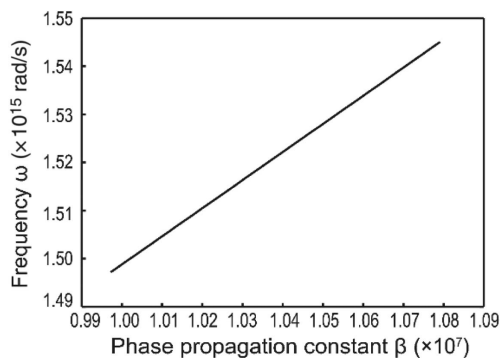


Fig. 10. Calculation for propagation speed, which is the ratio of the apparent change in ω to the associated change in β .

$$V_g \triangleq \frac{\partial \omega}{\partial \beta}, \quad (\text{D1})$$

where ω is frequency and β is the propagation constant of the propagating waveguide. The frequency-dependent β is calculated as shown in Fig. 10, where the range of frequency is from 1.497×10^{15} rad/s to 1.545×10^{15} rad/s (i.e., around the signal wavelength 1240 nm). Thus, V_g is calculated as a result of 5.846×10^7 m/s, and the propagation time in the modulation region is 21.21 fs. By contrast, the recovery time of the non-linear response in ITO is 360 fs [40]. Thus, the recovery time decides the modulation speed mostly, giving rise to a result of 2.78 THz.

Funding. National Natural Science Foundation of China (62005237); National Key Research and Development Program of China (2021YFB2801801).

Acknowledgment. H. Q. and H. M. conceived the idea. H. M. conducted the numerical simulations. H. M., D. L., and H. Q. contributed extensively to the writing of the manuscript. H. M., D. L., N. W., Y. Z., H. C., and H. Q. analyzed data and interpreted the details of the results. H. C. and H. Q. supervised the research.

Disclosures. The authors declare no competing interests.

Data Availability. The data that support the plots within this paper and other findings of this study are available from the corresponding author upon reasonable request.

REFERENCES

1. G. T. Reed, G. Mashanovich, F. Y. Gardes, and D. J. Thomson, "Silicon optical modulators," *Nat. Photonics* **4**, 518–526 (2010).
2. P. Minzioni, C. Lacava, T. Tanabe, J. Dong, X. Hu, G. Csaba, W. Porod, G. Singh, A. E. Willner, and A. Almazan, "Roadmap on all-optical processing," *J. Opt.* **21**, 063001 (2019).
3. D. A. Miller, "Attojoule optoelectronics for low-energy information processing and communications," *J. Lightwave Technol.* **35**, 346–396 (2017).
4. T. Hiraki, T. Aihara, K. Hasebe, K. Takeda, T. Fujii, T. Kakitsuka, T. Tsuchizawa, H. Fukuda, and S. Matsuo, "Heterogeneously integrated III–V/Si MOS capacitor Mach–Zehnder modulator," *Nat. Photonics* **11**, 482–485 (2017).
5. J.-H. Han, F. Boeuf, J. Fujikata, S. Takahashi, S. Takagi, and M. Takenaka, "Efficient low-loss InGaAsP/Si hybrid MOS optical modulator," *Nat. Photonics* **11**, 486–490 (2017).
6. M. He, M. Xu, Y. Ren, J. Jian, Z. Ruan, Y. Xu, S. Gao, S. Sun, X. Wen, and L. Zhou, "High-performance hybrid silicon and lithium niobate Mach–Zehnder modulators for 100 Gbit s^{−1} and beyond," *Nat. Photonics* **13**, 359–364 (2019).
7. M. Xu, M. He, H. Zhang, J. Jian, Y. Pan, X. Liu, L. Chen, X. Meng, H. Chen, Z. Li, X. Xiao, S. Yu, S. Yu, and X. Cai, "High-performance coherent optical modulators based on thin-film lithium niobate platform," *Nat. Commun.* **11**, 3911 (2020).
8. X. Guo, R. Liu, D. Hu, H. Hu, Z. Wei, R. Wang, Y. Dai, Y. Cheng, K. Chen, and K. Liu, "Efficient all-optical plasmonic modulators with atomically thin van der Waals heterostructures," *Adv. Mater.* **32**, 1907105 (2020).
9. M. Klein, B. H. Badada, R. Binder, A. Alfrey, M. McKie, M. R. Koehler, D. G. Mandrus, T. Taniguchi, K. Watanabe, and B. J. LeRoy, "2D semiconductor nonlinear plasmonic modulators," *Nat. Commun.* **10**, 3264 (2019).
10. O. Reshef, I. De Leon, M. Z. Alam, and R. W. Boyd, "Nonlinear optical effects in epsilon-near-zero media," *Nat. Rev. Mater.* **4**, 535–551 (2019).
11. R. Amin, R. Maiti, Y. Gui, C. Suer, M. Miscuglio, E. Heidari, R. T. Chen, H. Dalir, and V. J. Sorger, "Sub-wavelength GHz-fast broadband ITO Mach–Zehnder modulator on silicon photonics," *Optica* **7**, 333–335 (2020).

12. M. G. Wood, S. Campione, S. Parameswaran, T. S. Luk, J. R. Wendt, D. K. Serkland, and G. A. Keeler, "Gigahertz speed operation of epsilon-near-zero silicon photonic modulators," *Optica* **5**, 233–236 (2018).
13. X. Liu, K. Zang, J.-H. Kang, J. Park, J. S. Harris, P. G. Kik, and M. L. Brongersma, "Epsilon-near-zero Si slot-waveguide modulator," *ACS Photon.* **5**, 4484–4490 (2018).
14. C. M. Bender and S. Boettcher, "Real spectra in non-Hermitian Hamiltonians having PT symmetry," *Phys. Rev. Lett.* **80**, 5243–5246 (1998).
15. M.-A. Miri and A. Alu, "Exceptional points in optics and photonics," *Science* **363**, eaar7709 (2019).
16. T. Kato, *Perturbation Theory for Linear Operators* (Springer, 2013), Vol. 132.
17. Z.-P. Liu, J. Zhang, Ş. K. Özdemir, B. Peng, H. Jing, X.-Y. Lü, C.-W. Li, L. Yang, F. Nori, and Y.-X. Liu, "Metrology with PT-symmetric cavities: enhanced sensitivity near the PT-phase transition," *Phys. Rev. Lett.* **117**, 110802 (2016).
18. W. Chen, Ş. K. Özdemir, G. Zhao, J. Wiersig, and L. Yang, "Exceptional points enhance sensing in an optical microcavity," *Nature* **548**, 192–196 (2017).
19. H. Hodaie, A. U. Hassan, S. Wittek, H. Garcia-Gracia, R. El-Ganainy, D. N. Christodoulides, and M. Khajavikhan, "Enhanced sensitivity at higher-order exceptional points," *Nature* **548**, 187–191 (2017).
20. Y.-H. Lai, Y.-K. Lu, M.-G. Suh, Z. Yuan, and K. Vahala, "Observation of the exceptional-point-enhanced Sagnac effect," *Nature* **576**, 65–69 (2019).
21. B. Peng, Ş. K. Özdemir, F. Lei, F. Monifi, M. Gianfreda, G. L. Long, S. Fan, F. Nori, C. M. Bender, and L. Yang, "Parity-time-symmetric whispering-gallery microcavities," *Nat. Phys.* **10**, 394–398 (2014).
22. L. Shao, W. Mao, S. Maity, N. Sinclair, Y. Hu, L. Yang, and M. Lončar, "Non-reciprocal transmission of microwave acoustic waves in nonlinear parity-time symmetric resonators," *Nat. Electron.* **3**, 267–272 (2020).
23. H. Jing, S. Özdemir, X.-Y. Lü, J. Zhang, L. Yang, and F. Nori, "PT-symmetric phonon laser," *Phys. Rev. Lett.* **113**, 053604 (2014).
24. H. Hodaie, M.-A. Miri, M. Heinrich, D. N. Christodoulides, and M. Khajavikhan, "Parity-time-symmetric microring lasers," *Science* **346**, 975–978 (2014).
25. Z. Li, G. Cao, C. Li, S. Dong, Y. Deng, X. Liu, J. S. Ho, and C.-W. Qiu, "Non-Hermitian electromagnetic metasurfaces at exceptional points," *Prog. Electromagn. Res.* **171**, 1–20 (2021).
26. K. G. Makris, R. El-Ganainy, D. Christodoulides, and Z. H. Musslimani, "Beam dynamics in PT symmetric optical lattices," *Phys. Rev. Lett.* **100**, 103904 (2008).
27. S. Longhi, "Bloch oscillations in complex crystals with PT symmetry," *Phys. Rev. Lett.* **103**, 123601 (2009).
28. Y. Yan and N. C. Giebink, "Passive PT symmetry in organic composite films via complex refractive index modulation," *Adv. Opt. Mater.* **2**, 423–427 (2014).
29. L. Feng, Z. J. Wong, R.-M. Ma, Y. Wang, and X. Zhang, "Single-mode laser by parity-time symmetry breaking," *Science* **346**, 972–975 (2014).
30. H. Zhao, W. S. Fegadolli, J. Yu, Z. Zhang, L. Ge, A. Scherer, and L. Feng, "Metawaveguide for asymmetric interferometric light-light switching," *Phys. Rev. Lett.* **117**, 193901 (2016).
31. C. E. Rüter, K. G. Makris, R. El-Ganainy, D. N. Christodoulides, M. Segev, and D. Kip, "Observation of parity-time symmetry in optics," *Nat. Phys.* **6**, 192–195 (2010).
32. S. V. Suchkov, A. A. Sukhorukov, J. Huang, S. V. Dmitriev, C. Lee, and Y. S. Kivshar, "Nonlinear switching and solitons in PT-symmetric photonic systems," *Laser Photon. Rev.* **10**, 177–213 (2016).
33. M. Kulishov, J. M. Laniel, N. Bélanger, and D. V. Plant, "Trapping light in a ring resonator using a grating-assisted coupler with asymmetric transmission," *Opt. Express* **13**, 3567–3578 (2005).
34. Ş. K. Özdemir, S. Rotter, F. Nori, and L. Yang, "Parity-time symmetry and exceptional points in photonics," *Nat. Mater.* **18**, 783–798 (2019).
35. W.-P. Huang, "Coupled-mode theory for optical waveguides: an overview," *J. Opt. Soc. Am. A* **11**, 963–983 (1994).
36. A. Guo, G. Salamo, D. Duchesne, R. Morandotti, M. Volatier-Ravat, V. Aimez, G. Siviloglou, and D. Christodoulides, "Observation of PT-symmetry breaking in complex optical potentials," *Phys. Rev. Lett.* **103**, 093902 (2009).
37. J. Wiersig, "Enhancing the sensitivity of frequency and energy splitting detection by using exceptional points: application to microcavity sensors for single-particle detection," *Phys. Rev. Lett.* **112**, 203901 (2014).
38. P. Johnson and R. Christy, "Optical constants of transition metals: Ti, V, Cr, Mn, Fe, Co, Ni, and Pd," *Phys. Rev. B* **9**, 5056–5070 (1974).
39. A. D. Rakić, A. B. Djurišić, J. M. Elazar, and M. L. Majewski, "Optical properties of metallic films for vertical-cavity optoelectronic devices," *Appl. Opt.* **37**, 5271–5283 (1998).
40. M. Z. Alam, I. De Leon, and R. W. Boyd, "Large optical nonlinearity of indium tin oxide in its epsilon-near-zero region," *Science* **352**, 795–797 (2016).
41. J. H. Ni, W. L. Sarney, A. C. Leff, J. P. Cahill, and W. Zhou, "Property variation in wavelength-thick epsilon-near-zero ITO metafilm for near IR photonic devices," *Sci. Rep.* **10**, 713 (2020).
42. R. W. Boyd, *Nonlinear Optics* (Academic, 2020).
43. L. Zhang, A. M. Agarwal, L. C. Kimerling, and J. Michel, "Nonlinear group IV photonics based on silicon and germanium: from near-infrared to mid-infrared," *Nanophotonics* **3**, 247–268 (2014).
44. K. S. Rao, R. A. Ganeev, K. Zhang, Y. Fu, G. S. Boltaev, P. Krishnendu, P. V. Redkin, and C. Guo, "Laser ablation-induced synthesis and nonlinear optical characterization of titanium and cobalt nanoparticles," *J. Nanopart. Res.* **20**, 285 (2018).
45. A. Yariv, *Optical Electronics* (Saunders College Publishing, 1991).
46. J. Zhang, B. Peng, Ş. K. Özdemir, K. Pichler, D. O. Krimer, G. Zhao, F. Nori, Y.-X. Liu, S. Rotter, and L. Yang, "A phonon laser operating at an exceptional point," *Nat. Photonics* **12**, 479–484 (2018).
47. H. Park, S.-G. Lee, S. Baek, T. Ha, S. Lee, B. Min, S. Zhang, M. Lawrence, and T.-T. Kim, "Observation of an exceptional point in a non-Hermitian metasurface," *Nanophotonics* **9**, 1031–1039 (2020).
48. H. Hodaie, M. A. Miri, A. U. Hassan, W. Hayenga, M. Heinrich, D. Christodoulides, and M. Khajavikhan, "Parity-time-symmetric coupled microring lasers operating around an exceptional point," *Opt. Lett.* **40**, 4955–4958 (2015).
49. L. Wang, Y. Zhang, X. Guo, T. Chen, H. Liang, X. Hao, X. Hou, W. Kou, Y. Zhao, and T. Zhou, "A review of THz modulators with dynamic tunable metasurfaces," *Nanomaterials* **9**, 965 (2019).
50. R. Degl'Innocenti, S. J. Kindness, H. E. Beere, and D. A. Ritchie, "All-integrated terahertz modulators," *Nanophotonics* **7**, 127–144 (2018).
51. H. Qian, S. Li, C.-F. Chen, S.-W. Hsu, S. E. Bopp, Q. Ma, A. R. Tao, and Z. Liu, "Large optical nonlinearity enabled by coupled metallic quantum wells," *Light Sci. Appl.* **8**, 13 (2019).
52. H. Qian, S. Li, Y. Li, C.-F. Chen, W. Chen, S. E. Bopp, Y.-U. Lee, W. Xiong, and Z. Liu, "Nanoscale optical pulse limiter enabled by refractory metallic quantum wells," *Sci. Adv.* **6**, eaay3456 (2020).
53. L. Chen, Q. Xu, M. G. Wood, and R. M. Reano, "Hybrid silicon and lithium niobate electro-optical ring modulator," *Optica* **1**, 112–118 (2014).
54. M. Taghinejad, H. Taghinejad, Z. Xu, Y. Liu, S. P. Rodrigues, K. T. Lee, T. Lian, A. Adibi, and W. Cai, "Hot-electron-assisted femtosecond all-optical modulation in plasmonics," *Adv. Mater.* **30**, 1704915 (2018).
55. F. Cheng, C. Wang, Z. Su, X. Wang, Z. Cai, N. X. Sun, and Y. Liu, "All-optical manipulation of magnetization in ferromagnetic thin films enhanced by plasmonic resonances," *Nano Lett.* **20**, 6437–6443 (2020).
56. K. Wang, H. Qian, Z. Liu, and P. K. Yu, "Second-order nonlinear susceptibility enhancement in gallium nitride nanowires," *Prog. Electromagn. Res.* **168**, 25–30 (2020).
57. M. E. Ramon, A. Gupta, C. Corbet, D. A. Ferrer, H. C. Movva, G. Carpenter, L. Colombo, G. Bourianoff, M. Doczy, and D. Akinwande, "CMOS-compatible synthesis of large-area, high-mobility graphene by chemical vapor deposition of acetylene on cobalt thin films," *ACS Nano* **5**, 7198–7204 (2011).
58. M. Si, J. Andler, X. Lyu, C. Niu, S. Datta, R. Agrawal, and P. D. Ye, "Indium-tin-oxide transistors with one nanometer thick channel and ferroelectric gating," *ACS Nano* **14**, 11542–11547 (2020).
59. S. Ellingson, *Electromagnetics* (Virginia Tech Libraries, 2018), Vol. 1.